Origins of Improved Carrier Multiplication Efficiency in Elongated Semiconductor Nanostructures

Journal:	*Physical Chemistry Chemical Physics*
Manuscript ID:	CP-ART-08-2014-003706.R2
Article Type:	Paper
Date Submitted by the Author:	02-Dec-2014
Complete List of Authors:	Sills, Andrew; University of Leeds, School of Electrical & Electronic Engineering Califano, Marco; University of Leeds, The School of Electronic and Electrical Engineering

Physical Chemistry Chemical Physics
CREATED USING THE RSC LaTeX PCCP ARTICLE TEMPLATE – SEE www.rsc.org/electronicfiles FOR DETAILS
ARTICLE TYPE www. rsc.org/xxxxxx | XXXXXXXX

Origins of Improved Carrier Multiplication Efficiency in Elongated Semiconductor Nanostructures†

Andrew Sills,*[b‡] and Marco Califano[a]

Received Xth XXXXXXXXXX 20XX, Accepted Xth XXXXXXXXX 20XX
First published on the web Xth XXXXXXXXXX 200X
DOI: 10.1039/b000000x

Nanorod solar cells have been attracting a lot of attention recently, as they have been shown to exhibit a lower carrier multiplication onset and a higher quantum efficiency than quantum dots with similar bandgaps. The underpinning theory for this phenomenon is not yet completely understood, and is still the subject of ongoing study. Here we conduct a theoretical investigation into CM efficiency in elongated semiconductor nanostructures with square cross section made of different materials (GaAs, GaSb, InAs, InP, InSb, CdSe, Ge, Si and PbSe), using a single-band effective mass model. Following Luo, Franceschetti and Zunger we adopt the CM figure of merit (the ratio between biexciton and single-exciton density of states) as a measure of CM efficiency and investigate its dependence on the aspect ratio for both (a) constant cross section (i.e. varying the volume) and (b) constant volume (i.e., varying the cross section), by decoupling electronic structure effects from surface-related effects, increased absorption and Coulomb coupling effects. The results show that in both (a) and (b) cases elongation causes an increase in both single- and bi-exciton density of states, with the latter, however, growing much faster with increasing energy. This leads to the availability of more bi-exciton states than single-exciton states for photon energies just above the bi-exciton ground state and therefore suggests a higher probability of CM at these energies for elongated structures. Our results therefore show that the origin of the observed decrease of the CM threshold in elongated structures can be attributed purely to electronic structure effects, paving the way to the implementation of CM-efficiency-boosting strategies in nanostructures based on the lowering of the CM onset.

1 Introduction

In conventional photovoltaic devices, the absorption of a photon always creates a single pair of oppositely charged particles (electrons and holes), regardless of the photon energy. In a semiconductor nanocrystal (NC) of a suitable material, multiple electron-hole pairs can be generated upon the absorption of a single high-energy photon, their number depending only on the photon energy[1]. Thanks to this process, called carrier multiplication (CM), or multiple exciton generation (MEG), a more efficient and complete conversion of solar energy into electric current could be achieved in a NC-based solar cell[2] and at the same time the detrimental heat generation that accompanies conventional conversion could be reduced.

Unfortunately, despite experimental confirmation of CM in a wide range of materials[3–7], CM-based solar cells are still far from yielding multiplication factors even close to 2 (i.e., the best recorded internal quantum efficiencies are still far from 200%)[8,9]. What is more, the mechanism behind CM itself is still unclear and many aspects of it remain controversial. In particular it has been observed experimentally that elongated nanostructures exhibit higher CM efficiencies which are associated with lower CM onsets. The origins of this effect are however not clear. Multiple factors could be responsible for it: (i) the larger volume of the rod, when compared with a spherical structure with the same band gap, leading to a larger absorption cross section, (ii) a larger surface-to-volume ratio, leading to an increase in surface-related effects (such as ligand- or trap-mediated processes or other environmental effects), (iii) a different electronic structure leading to an increased (biexcitonic) density of states (DOS), (iv) the enhanced Coulomb coupling that binds electrons and holes into well defined 1D excitons , leading to bimolecular (i.e., two-body) Auger interactions between the two excitons in rods[10], compared to the three-body interactions between free carriers in spherical NCs[11], or some other unknown cause. Here we investigate the possible origins of the observed lowering of the CM onset by decoupling electronic structure effects (iii) from surface-related effects (ii), absorption effects (i), and effects due to enhanced Coulomb interaction (iv). By using a single-band effective mass model with an infinite potential barrier, we prevent the carriers wave functions from sampling the surface, effectively removing surface effects (ii) from the calculation. At the same time this approach allows us to investigate a range of elongations otherwise inaccessible to more accurate atomistic approaches, due to the prohibitively large number of atoms involved. By describing excitons in the single-particle picture, where $E(X) = E(e_i) + E(h_j) + E_g^{\text{bulk}}$ (see (2)), we

neglect enhancement effects of the Coulomb interactions between electrons and holes due to confinement, excluding (iv). We then consider the single- and bi-exciton DOS following the absorption of a single high-energy photon, thereby excluding possible effects due to variations in the absorption cross section (i). We finally compare the effect of elongations at constant cross section with that of elongation at constant volume. We find that as the aspect ratio (i.e., the elongation) of the structure increases, so does the single-particle DOS in both the valence and the conduction bands. This leads to an increase in both single- and bi-exciton densities of states, with the latter increasing at a faster rate, though, causing a decrease in the energy E_0 at which the two curves cross (which is closely related to the energy position of the CM onset). This effect is important as a lowering of the CM onset is associated with increased CM efficiency [12,13] and enhanced solar energy conversion [14,15].

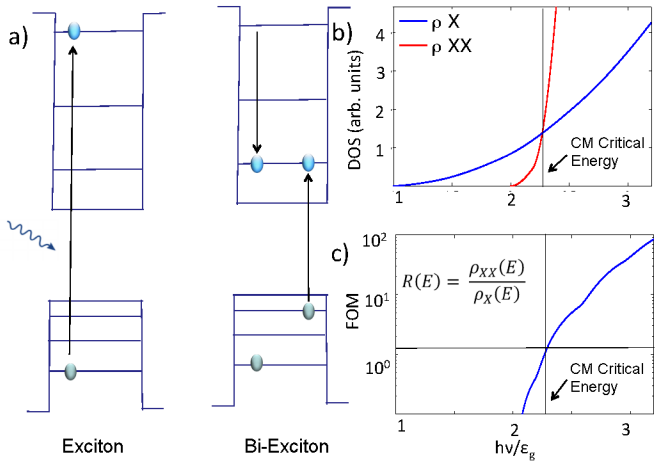

Fig. 1 (a) Schematics of CM via impact ionisation. (b) Density of single exciton (blue) and bi-exciton (red) states versus energy for cubic GaAs NCs with sides of 10 lattice constants. (c) Ratio of red and blue curves in (b) plotted on a logarithmic scale to show a figure of merit characteristic.

In 0D confined structures, CM is typically described in terms of impact ionisation (II) [1,3,16–18], a term originally used to describe this process in bulk materials: the photon energy in excess of the bandgap, rather than being lost to the lattice in the form of phonons, can be transferred by one of the two photogenerated carriers to an electron in the valence band, exciting it to the conduction band, and creating a further exciton (for a total of two excitons generated per absorbed photon, see Fig. 1a). For CM to take place the photon energy must be at least twice the bandgap (i.e., the excess energy of the carrier at least equal to E_g), the minimum energy required to create a ground state bi-exciton (the minimum energy to excite a second valence electron across the band gap). The inverse process, where a bi-exciton (XX) recombines to form an exciton (X) is referred to as Auger recombination (AR). Both processes are governed by the same transition matrix elements. This identity is indeed the reason why impact-ionisation had been previously dismissed [19,20] as the source of CM in NCs, based on the then perceived incompatibility between the ~ 10 ps AR lifetimes and the observed < 400 fs CM decay. The crucial difference between the two processes, however, is that the initial states in the former represent the final states in the latter and *vice versa*.

It has been shown that the II rate is proportional to the number of available final (i.e., XX) states [16–18] and the AR rate to the number of final X states [21]: CM can therefore be much faster than AR when the density of bi-exciton states $\rho_{XX}(E)$ is greater than the density of single exciton states $\rho_X(E)$ (see Fig. 1b). The ratio $R(E) = \rho_{XX}(E)/\rho_X(E)$, referred to as the CM figure of merit (FoM) [22], is therefore an important parameter in the determination of the efficiency of CM in NCs. Ideally, for photovoltaic applications, this ratio should be greater than one, implying a higher rate of II than AR. At the same time, smaller values of $\rho_X(E)$ could be indicative of a reduction in the efficiency of phonon-assisted relaxation, the main mechanism competing with II. Indeed, tight-binding calculations [18] have shown that at high energies impact ionisation rates are comparable in bulk and nanostructured PbSe, which may suggest that the increase in efficiency caused by the relaxation of momentum conservation rule in the latter may be compensated by a reduced efficiency in phonon-assisted decay, due to a sparser density of electronic levels.

The importance of $R(E)$ has also been confirmed by the results of recent ab-initio time-dependent density functional theory calculations combined with non-adiabatic molecular dynamics [23], which interestingly also showed that multiple exciton *recombination* (AR) is only possible for energies in the window $2E_g \leq E < 3E_g$, i.e., close to the crossing point between $\rho_{XX}(E)$ and $\rho_X(E)$. An alternative model proposed by Klimov explains CM in terms of direct generation of multiexcitons via Coulomb coupling to virtual single-exciton states [19]. In this model the CM efficiency depends on the ratio of the biexciton and single exciton generation rates, and therefore on $R(E)$.

Following the convention, [17,18,22] we define the CM critical energy E_0 as the energy at which $R(E) = 1$ (Fig. 1c). Above this energy CM rates are larger than AR rates, i.e., bi-exciton generation becomes faster, leading to more efficient carrier multiplication. The CM onset E_{onset} is defined as [17] $\max(E_0, E_{\text{opt}})$, where E_{opt} is the minimum photon energy such that either of the photogenerated carriers has sufficient energy to initiate CM. In this work we will be concerned with possible strategies to engineer the critical energy E_0. In particular, we will show that experimental observations of lower CM onsets

in elongated nanostructures correlate with theoretical predictions of reduced values for E_0, thereby establishing a close correspondence between critical energy and CM efficiency.

While the size-tunability of the band-gap is well established in NCs, a model for the tunability of the CM onset requires a careful consideration of the band-structure and in particular of the distribution of states just above the bi-exciton ground state energy $2E_g$. A theoretical study on the effects of the band structure on CM efficiency was conducted by Luo *et al.*[22] using the infinite-barrier truncated-crystal approximation (TCA) within the semi-empirical pseudopotential method. They calculated the CM FoM for *cubic* NCs of different sizes (l=6a_0, 8a_0 and 10a_0, where a_0 is the lattice constant), made of different materials, and found that it was larger for PbSe, Si, GaAs, CdSe, and InP, suggesting a lower CM onset and therefore higher efficiency for these materials. They concluded that high CM efficiency requires high degeneracy in the bulk band-edge states. As a consequence of its peculiar electronic structure[24], where both CBM and VBM are located at the 4-fold degenerate L-point, PbSe was shown to have the highest CM FoM. Conversely, InAs was found to have one of the lowest efficiencies, from this point of view, given its large Γ-L and Γ-X spacings in the bulk, which prevent any confinement-induced Γ-to-L and Γ-to-X electronic transitions in small NCs. In other materials (such as GaAs, InSb, and GaSb), small Γ-L spacings in the bulk cause the electron states to derive from the L-point Bloch state, in sufficiently small NCs, leading to larger CM efficiencies.

Since the publication of Luo's work, advances in colloidal synthesis techniques have paved the way for the manufacture of cubic nanostructures (cubic quantum dots and square-sectional quantum rods) for a variety of semiconductors of different sizes[25–28] using self assembly techniques. Interestingly, cubic structures have been shown to have a higher packing density than spherical dots[29]. This could lead to more highly efficient devices sitting on the same substrate, and therefore harnessing even more energy from sunlight. Furthermore, although experimentally the CM onset has been shown to be independent of the NC size, for spherical NCs of a specific material[14,30], it has recently been found to depend on the NC *shape*[31–35]. Therefore further theoretical and experimental work is required on this subject[36] to shed light on these experimental findings.

One interesting line of enquiry would be an investigation into the effects of elongation. Unlike in spherical or cubic structures, where electrons and holes experience equal quantum confinement in all three spatial dimensions, in an elongated structure the confinement is relaxed along one dimension, creating a quasi one dimensional system where the bandgap is largely determined by the smaller dimensions. However, as the elongation increases, the decrease in the confinement energy along that direction reduces the energy spacing between neighbouring states, increasing the DOS in both valence and conduction bands.

Klimov's group was the first to show experimental evidence to support the claim that the CM onset is a useful parameter in determining the CM efficiency for PbSe NCs[12], further emphasizing the importance of the former being as close to $2E_g$ as possible[36]. More recent experimental studies investigating the behaviour of this characteristic in quantum rods have observed a general reduction in the CM onset for PbSe quantum rods compared to their dot-like siblings with similar bandgaps. However, the energy value to which the onset converges with elongation and the aspect ratio at which convergence is achieved are still controversial[32–34]. Cunningham et al.[32] measured an increase of CM efficiency and a concomitant reduction of E_{onset} from 2.9 to 2.33 for aspect ratios increasing from 1 to 4-5 in cylindrical structures with a diameter of 4.4 nm, while Sandberg et al.[33] observed a decrease from 3.2 to 2.6 in the electron-hole pair creation energy for aspect ratios reaching up to 7-8, albeit in narrower structures, with typical diameters of 3-3.6 nm.

This strong interest in PbSe nanostructures originates from a number of reasons. Firstly the bandgap is small enough to allow CM for low energy photons corresponding to the infrared region of the electromagnetic spectrum. Secondly, the unique band structure gives an extra 4-fold degeneracy in both conduction and valence band edges[24]. Also, the relatively large dielectric constant causes a reduction in carrier-carrier interactions, leading to an increase in the exciton Bohr radius, which can, in theory, be up to the length of the rod[10]. However nanostructures made of a number of other materials may offer alternative advantages: e.g., ease of integration with existing Si-based technology (Si and Ge), more ideally placed bandgap for solar absorption (InAs, InSb), more mature colloidal technology (CdSe, CdS), etc. We therefore decided to screen a large sample of different materials.

We aim to first validate our method by comparing its results for non-elongated structures with the CM critical energies calculated by Luo *et al.*[22]. We will therefore consider cubic NCs with the same dimensions as those used in reference[22], which, as mentioned above, are now experimentally accessible in a variety of semiconductor materials and in different sizes.[25–28]

2 Methods

The electronic structure in both the conduction (CB) and valence band (VB) is calculated using the eigenvalues solutions of the Schrödinger equation for a quantum box with an infinite confining potential (the charge distribution of the 6 lowermost states is shown in Fig. 2a):

$$E_{i,j,k}^{CB,VB} = \frac{\hbar^2\pi^2}{2m_{e,h}^*}\left(\frac{i^2}{L_x^2}+\frac{j^2}{L_y^2}+\frac{k^2}{L_z^2}\right) \quad (1)$$

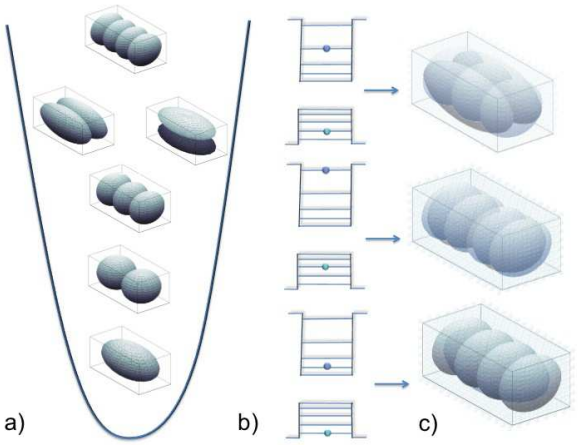

Fig. 2 (a) The charge density of the 6 states closest to the band edge (111, 112, 113, 121, 211, 114) for a nanorod with aspect ratio 2. (b) Possible single-exciton configurations and (c) their corresponding charge distributions.

where the effective mass parameters listed in table 1 were used. In order to make sure that all energy levels within a specific energy window $[E_{min}, E_{max}]$ are included in the calculated DOS, a maximum quantum number n^{max} $(n = i, j, k)$ is pre-calculated, defined as the highest quantum number yielding an energy within the window while the other two $(m, l \neq n)$ are set to one. e.g. $E_{1,1,k^{max}} < E_{max}$ and $E_{1,1,k^{max+1}} > E_{max}$.

The single-exciton energies E_X are then obtained as

$$E_{i,j,k}^{X} = E_{i,j,k}^{CB} + E_{i,j,k}^{VB} + E_g^{\text{bulk}} \quad (2)$$

where E_g^{bulk} is the bulk band gap for the given semiconductor material (possible single-exciton configurations are schematically shown in Fig. 2b in the single-particle picture, together with their charge density - Fig. 2c). In our approach we therefore neglect (a) higher energy bands (such as the L valleys in GaAs, GaSb and InSb), (b) band anisotropies, and (c) excitonic effects, the most important of which is the red shift of the band edge due to electron-hole Coulomb attraction. Furthermore, the infinite potential is known to overestimate the confinement energy, as in reality there is a finite probability of the carriers to exist in the barrier. One possible strategy to compensate for this, is to model the structure as being slightly larger than its actual dimensions. Bryant *et al.*[37] showed that a better agreement with the measured optical gaps could be achieved by assuming $L' = 1.3L$, where L' is the overestimated cross sectional width of the dot. Here we choose not to follow this route and let the reader decide which size to use in the comparison with experiment (indeed the ratio between two consecutive sizes considered in this work - $6a_0$, $8a_0$ and $10a_0$ - is nearly 1.3). It has been suggested[22] that the inclusion of higher valleys [point (a) above] is important in the calculation of the DOS. However, here we are mainly concerned with the determination of the energy E_0 at which the *ratio* between the DOS is equal to 1. This quantity may be less sensitive to the details of the band structure at high energy. Indeed our calculated values for E_0 show a reasonable agreement with the results of the TCA (see Fig. 8 below), where the effects of higher bands are properly taken into account[22].

This result therefore provides a validation *a posteriori* of our simple approach.

	m_e	m_h	$E_g(eV)$
GaAs	0.067	0.45	1.52
GaSb	0.041	0.4	0.81
InAs	0.023	0.41	0.42
InP	0.43	0.6	1.43
InSb	0.25	0.41	0.24
CdSe	0.13	0.43	1.75
Si	0.328	0.49	1.13
Ge	0.2194	0.33	0.74
PbSe	0.058	0.054	0.28

Table 1 Parameters used in the present calculations. For highly anisotropic semiconductors such as Si, Ge and PbSe the reported value is the average between longitudinal (m_l) and transverse (m_t) masses, according to the following expression $m^* = \sqrt[3]{m_l^2 m_t}$.

The electronic structure of semiconductor nanocrystals has been previously investigated using a variety of theoretical approaches: (i) effective mass models and $k \cdot p$ methods[38–41], often provide analytical solutions which are easier and more intuitive to understand than the numerical results of atomistic methods, such as (ii) the tight-binding method[42–47], (iii) the semi-empirical pseudo-potential method,[48,49], and (iv) fully self-consistent *ab-initio* methods, based on density functional theory[50–57].

One advantage of the continuum single-band effective mass approach over atomistic methods is computational simplicity: the latter can become expensive when simulating very large structures such as nanorods, containing tens of thousands of atoms. Another attractive aspect of this choice is the possibility of completely decoupling the NC core from its surface in the calculations and therefore isolating electronic structure effects from possible environmental effects (such as interactions at the surface with ligands, unsaturated bonds, and the solvent), by using infinite potential barriers which prevent the carriers' wave functions from sampling the nanostructure's surface.

We are interested in the densities of exciton and bi-exciton

states within the energy range $2E_g<E<3E_g$, i.e., just above the energy threshold for biexciton generation, but excluding higher order multi-excitons. In their determination, it is important to consider Pauli's exclusion principle for each exciton and bi-exciton state. For example, while determining the degeneracy of a single exciton $X_{\alpha,\beta} = |e_\alpha;h_\beta\rangle$ [where e_α (h_β) is the electron (hole) state $\alpha = i,j,k$ ($\beta = h,l,m$), solution of (1)] is simple (it is always four, including pseudo-spin), the case of a bi-exciton $XX_{\alpha,\beta,\gamma,\delta} = |e_\alpha,e_\beta;h_\gamma,h_\delta\rangle$ is slightly more complicated and depends on whether the two electrons in the CB and the two holes in the VB are in the same state or not (i.e, whether or not $\alpha = \beta$ and/or $\gamma = \delta$).

Once the energies and degeneracies of exciton and bi-exciton states have been calculated for both cubic and elongated structures, the FoM $R(E)$ is obtained as the ratio of their DOS (Fig. 1c). The energy at which $R(E) = 1$ (the point where the curves $\rho_{XX}(E)$ and $\rho_X(E)$ intersect, see Fig. 1b) is then obtained for several values of the aspect ratio, keeping either a constant cross section (and varying the volume) or a constant volume (and varying the cross section).

Luo *et al.*[22] pointed out that, since the Coulomb operator in the Auger matrix elements only couples states that differ by no more than two particles, one should consider the ratio $\rho_{XX}(\varepsilon,E)/\rho_X(\varepsilon,E)$, between the biexciton and exciton DOS, where *one carrier is fixed* in the single-particle level at energy ε. This led them to introduce the quantity

$$R_2(E) = \frac{1}{N(E)} \int_{\varepsilon_{\min(E)}}^{\varepsilon_{\max(E)}} \rho(E) \frac{\rho_{XX}(\varepsilon,E)}{\rho_{X(\varepsilon,E)}} d\varepsilon \qquad (3)$$

as CM figure of merit. The results of their calculations, however, show little difference between the curves $R(E)$ (which neglects the Coulomb selection rule) and $R_2(E)$ for most materials, especially regarding the energy E_0 at which they are equal to 1. As the determination of such an energy is the main focus of our investigation, for the sake of simplicity we will therefore neglect Coulomb selection rules and consider R.

The single-particle DOS calculated for VB and CB are shown in Fig. 3. Most of the simulated semiconductor NC structures have a larger DOS in the VB than in the CB. Due to the very small electron effective mass in InAs, the DOS in the CB of nanocubes made of this material is very low, whereas the symmetric band structure we obtain for PbSe is a consequence of the roughly similar electron and hole effective masses used in the calculation (see Table 1). InP NCs appear to have the highest DOS in both bands, while at the same time having a relatively large band gap.

Compared to the cubic NCs shown in Fig. 3, a fourfold increase in volume (aspect ratio) yields, for most materials, a decrease in the bandgap similar to (or smaller than) that obtained with a 25% increase in the cube size, with, however, a much larger increase in the corresponding density of states

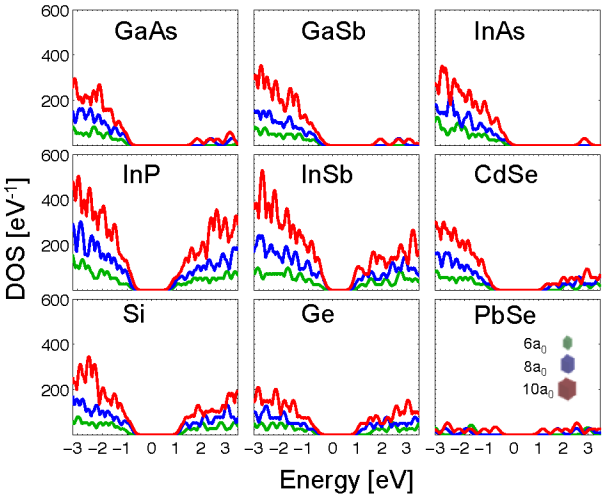

Fig. 3 The single-particle density of states for cubic NCs of different materials (GaAs, GaSb, InAs, InP, InSb, CdSe, Ge, Si and PbSe) for three different dot sizes (red $L = 10a_0$, blue $L = 8a_0$, and green $L = 6a_0$, where a_0 is the lattice constant and L is the length of the cube).

in the elongated structures, particularly significant at the band edges.

Starting from these single-particle DOS we then calculated the single- and bi-exciton DOS, and finally the CM FoM.

Before presenting the effects of elongation on the CM critical energy, we will validate our method by comparing its results for cubic structures (i.e. aspect ratio = 1) with those obtained with the truncated crystal approximation[22]. Our calculated CM FoM are displayed in Fig. 5 (solid lines) for all materials considered, as a function of the excitation energy: our results show a clear size dependence in most of the cases, except for InAs and PbSe, in good agreement with observations in these two systems[15,30]. This lack of size dependence is due in InAs to the extremely sparse conduction band: a much larger increase in size than what we consider here would be required to access higher energy levels in this band.

The results of TCA are presented in Fig. 5 as dashed lines. The two approaches predict similar trends for the CM FoM as a function of photon energy in most of the materials considered (with some quantitative differences at the boundaries of the energy region of interest), except in the case of InAs, where TCA predicts a more marked size dependence, in contrast with experiment[15]. On the other hand our calculations predict a clear size dependence for CdSe NCs, in contrast with TCA and experiment[5].

The FOM for PbSe shown in Fig. 5 was obtained using the solutions of (1), i.e., without accounting for the extra degeneracy of the bulk band edges in this material. The effect of this degeneracy is illustrated in Fig. 6, where 3 extra states were

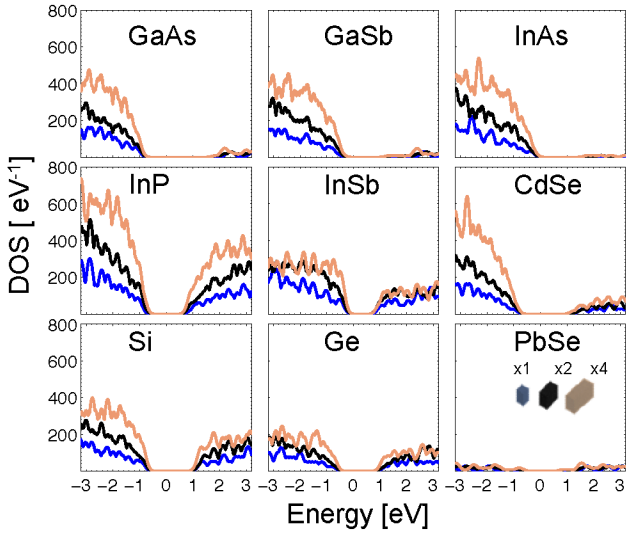

Fig. 4 The single-particle density of states for square cross-section nanorods of different materials (GaAs, GaSb, InAs, InP, InSb, CdSe, Ge, Si and PbSe) for three different aspect ratios (1, blue line; 2, orange line; and 4, black line) with a constant cross section of $8a_0^2$, where a_0 is the lattice constant. Compared to the cubic NCs shown in Fig. 3, a fourfold increase in volume (aspect ratio) yields, for most materials, a decrease in the bandgap similar to (or smaller than) that obtained with a 25% increase in the cube size, with, however, a much larger increase in the corresponding density of states, particularly significant at the band edges.

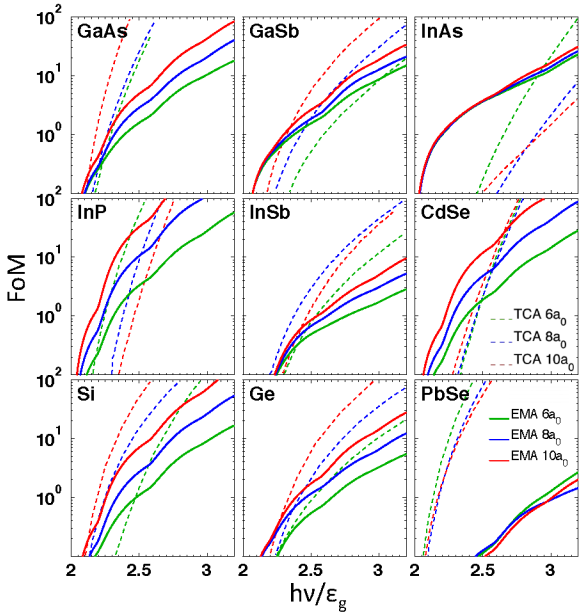

Fig. 5 Figure of Merit characteristics for cubic NCs of different materials (GaAs, GaSb, InAs, InP, InSb, CdSe, Ge, Si and PbSe) for three different dot sizes ($L = 10a_0$, red lines; $L = 8a_0$, blue lines; and $L = 6a_0$, green lines. a_0 is the lattice constant and L is the length of the cube). Solid lines: present work; dashed lines TCA [22].

added by hand at the band edges, to simulate the 4-fold degenerate L states in bulk PbSe (for consistency with our method (1), the results presented below were all obtained without including this "artificial" degeneracy). Our calculated CM critical energy in Fig. 5 shows better agreement with the experimentally determined CM onset[3], compared to that obtained using TCA, whereas the value of E_0 presented in Fig. 6 shows a closer comparison to the TCA results.

Most of the FoM characteristics shown in figure 5 compare reasonably well with the TCA, in particular for energies close to $2E_g$. We find that for most semiconductors the CM critical energy is closer to $2E_g$ for larger structures and shifts to increasingly larger values with decreasing size, following the expected decrease in the single-particle DOS.

However, an inverse size dependence can also occur, i.e. larger dots can exhibit a reduced E_0 with an increase in size. This can happen in strongly confined systems, when the decrease in bandgap has a greater effect than the increase in the DOS, causing an overall reduction of the number of states in the window of opportunity $2E_g < E < 3E_g$. For the work presented here only PbSe,(exciton Bohr radius in the bulk $R_{\mathrm{Bohr}} = 46$ nm), shows this inverse size dependence, while the CM critical energy calculated for InAs is size-independent. In the work reported by Luo *et al.*[22], instead, this inverse size dependence was found in InP and to a lesser extent also in PbSe and InAs (in both of which complete inversion occurred only after intersection with the $R(E) = 1$ line, see Fig. 5) and InSb (where only the two curves relative to the largest sizes were found in reverse order). If strong confinement were the only origin of this effect, then, using the value of the bulk exciton Bohr radius as an estimate of it, we would expect InSb (which has the largest value of R_{Bohr} among the materials considered), to exhibit the most marked inverse size dependence, followed (with decreasing values of R_{Bohr}[58]) by PbSe, InAs, GaSb, InP and so on. However, as this is not the order found in neither our calculations nor in those performed by Luo *et al.*[22], we speculate that other properties (such as the value of electron and hole effective masses and their ratio) play an important role in determining the actual size dependence. To confirm this we re-calculated the FoM for: (a) InAs using two different hole effective mass values about one order of magnitude smaller than the actual ones and similar to that of the electron ($m_h = 0.02m_0 \lesssim m_e$ and $m_h = 0.04m_0 > m_e$); (b) GaSb with $m_h = 0.04m_0$ (i.e., 10 times smaller than the correct value and $\sim m_e$); and (c) PbSe using $m_h = 0.54m_0$ (i.e., 10 times larger than the correct value and than m_e). We find (see Fig. 7) (a1) a complete inverse size dependence for InAs if $m_h \sim m_e$ and $m_e/m_h \gtrsim 1$; (a2) a photon-energy-dependent

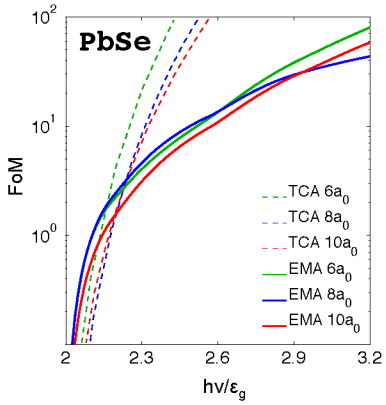

Fig. 6 PbSe FoM: Same as in figure 5, with the extra 4 fold degeneracy at the band edges included.

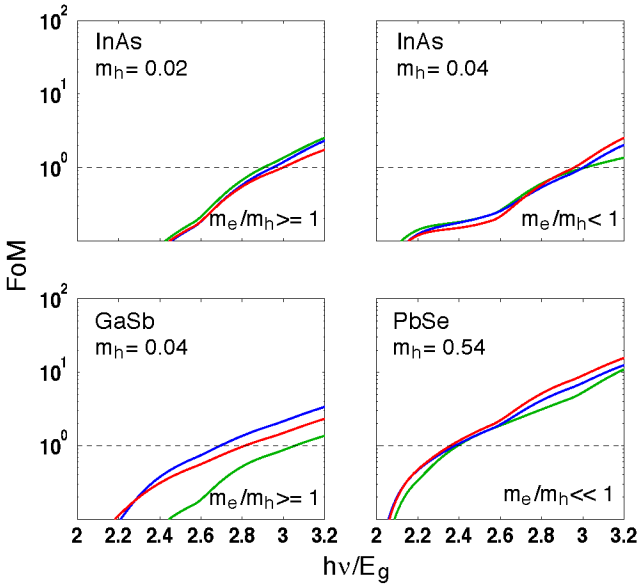

Fig. 7 Recalculated FoMs for InAs, GaSb and PbSe using the same parameters as in figure 5, with the exception of the value of the hole effective mass (reported in the plots).

behavior if $m_h \sim m_e$ and $m_e/m_h < 1$, where smaller sizes have larger FoM (i.e., an inverse size dependence) for $h\nu \lesssim 2.7E_g$ and then the dependence on size is reversed, becoming "normal" for photon energies above $3E_g$; (b) a partial inversion in GaSb for $m_h \sim m_e$ and $m_e/m_h \gtrsim 1$; and (c) a normal size dependence for PbSe when $m_h \gg m_e$ and $m_e/m_h \ll 1$. As expected the CM critical energy approaches $3E_g$ as the effective mass ratio approaches 1.

The most important question is, however: how well can EMA approximate the results of TCA regarding the position of the CM *critical energy*? This is, in fact, the quantity we will focus on in elongated structures. A detailed comparison of the CM critical energies obtained with the two methods is presented in Fig. 8, where for PbSe we report the results from Fig. 5 (i.e., without the additional 4-fold degeneracy of the band edges used in Fig. 6), as this is the set we will use in our elongated structures calculations. The agreement is generally quite good for all materials and NC sizes, except for InAs and PbSe (and, to some extent, InSb) which are also the materials that exhibit the weakest agreement for the calculated bandgaps (not shown).

Having established the reliability of our calculated CM critical energies for cubic structures, we can now proceed to investigate the effects of increasing nanocrystal elongation. The variation of E_0 as a function of aspect ratio is presented in Fig. 9 for elongations at constant cross section, and in Fig. 10 for elongation at constant volume. The former case reflects the experimental conditions in which preferential growth along one direction is achieved, maintaining the cross section unaltered and resulting in an almost constant band gap, whereas the latter case allows us to remove all possible volume-scaling effects, by keeping the volume constant and therefore varying both cross section and band gap. The general trend looks qualitatively similar in the two cases, the CM critical energy decreasing with elongation, but exhibiting a faster convergence at constant cross section, for most materials. A closer inspection of Fig. 9 reveals, however, a remarkable material-dependent behavior: GaAs, GaSb, InP, CdSe, Si and Ge exhibit a marked size-dependence of the aspect ratio $\sigma_{\min}$ at which E_0 converges to the minimum value of the CM onset (theoretically $2E_g$). In these materials, $\sigma_{\min}$ ranges from about 2 (in InP) to 5 (in Ge and GaSb) for the largest structures, and from about 6 (in CdSe) to ~ 10 (in Ge), and even > 10 (see below), for the smallest rods, and is always inversely proportional to the rod size. For InAs, InSb and PbSe, $\sigma_{\min}$ is instead size-independent. In the case of PbSe rods with $L = 8a_0$ (4.9 nm) we predict a decrease of the CM critical energy from $\sim 3.0E_g$ to $\sim 2.25E_g$ for an increase of σ from 1 to 4, in good agreement with the experimental results of Cunningham et al.[32] who observed a reduction of E_{onset} from 2.9 to 2.33 for aspect ratios increasing from 1 to 4-5 in nanorods with typical diameters of 4.4 nm. Furthermore, our predicted size independence for $\sigma_{\min}$ is consistent with the recent findings of a diameter-independent maximum for the CM yields observed at aspect ratios of about 8[35]. Indeed, according to our results, the CM threshold does not exhibit any further decrease (hence the CM efficiency is not expected to further increase) with increasing values of σ beyond about 9 (which value is also in fair agreement with experiment). Our predicted value for the CM critical energy of a $L = 6a_0$ (3.7 nm) rod with $\sigma = 8$ ($\sim 2E_g$) is, instead, in disagreement with the data reported by Sandberg et al.[33], who find a reduction of the electron-hole

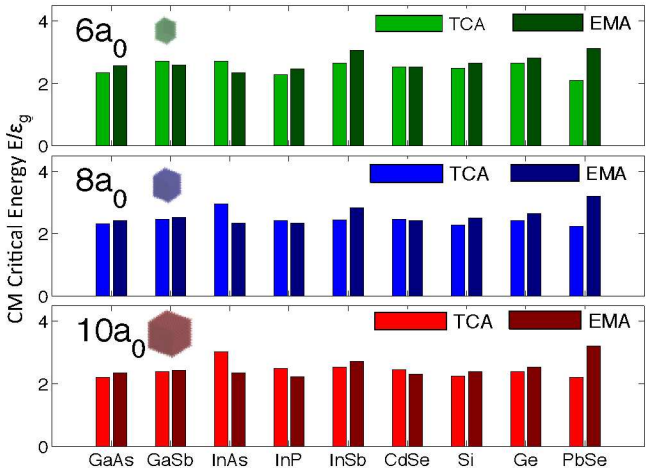

Fig. 8 A comparison of the CM critical energies E_0 (with $R(E_0) = 1$) obtained from Fig. 5 for effective mass vs TCA. The color coding follows the same convention as Fig. 5, i.e., light and dark green: $6a_0$, light and dark blue: $8a_0$, and light and dark red: $10a_0$.

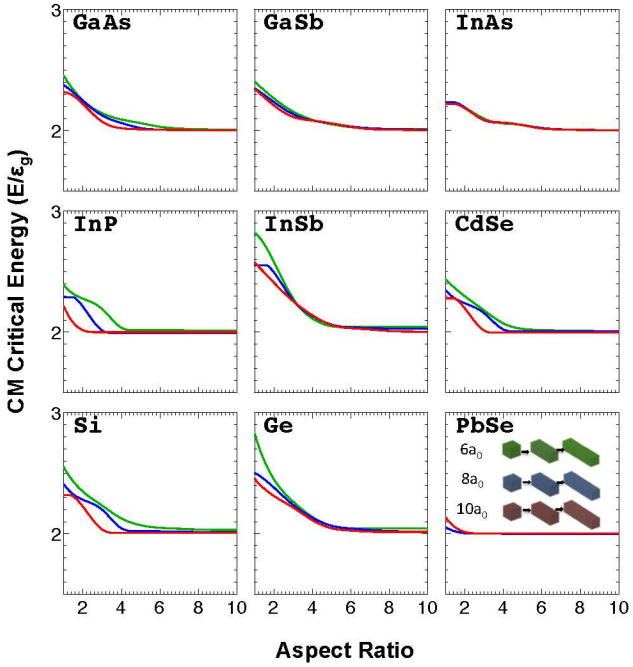

Fig. 9 Variation of (normalized) CM critical energies as a function of aspect ratio at constant cross section calculated for three different widths $6a_0$, $8a_0$ and $10a_0$.

pair creation energy from $\sim 3.2E_g$ to $\sim 2.6E_g$ with elongation to $\sigma = 7 \div 8.4$ for rods with average radii of 3 and 3.6 nm.

Interestingly we also find that in some materials (InP and Si) the value of E_0 for the smallest structure does not converge to the theoretically expected value of $2E_g$ for any value of the aspect ratio considered (up to 10), requiring structures longer than $60a_0$ (37 nm) to reach it.

In the case of elongation at constant volume (Fig. 10), we find that for all materials (except PbSe) the CM critical energy converges at much higher values of σ, compared to the case of elongation at constant cross section, with $\sigma_{\min}$ generally larger than 6 for all rod sizes considered. In this case only InP shows a size-dependent $\sigma_{\min}$ and E_0 does not converge to $2E_g$ for a larger number of materials (InP, CdSe, Si and Ge). These different features observed in Fig. 10 compared with Fig. 9 can be explained in terms of the competition between the opposite effects on the DOS caused by increased elongation (i.e., deconfinement) along one direction (which leads to an increase in the DOS), and increased confinement in the perpendicular plane (which decreases the DOS), combined with the behavior of the bandgap as a function of aspect ratio in the two cases. For elongation at constant volume (i.e., when the cross section is reduced), the increase in confinement along the two shorter axes would lead to a decrease in the DOS, which is balanced by the large increase of both bandgap and elongation. For elongations at constant cross section, instead, there is no increase in confinement, and the decreased confinement along the structure long axis leaves the bandgap largely unchanged, after an initial small drop (materials with large bulk bandgaps, such as CdSe, exhibit the smallest decrease). In the latter case, therefore, the CM critical energy converges at lower aspect ratios than in the former.

3 Conclusions

A continuum approach was used to model the band structure of cubic NCs of different materials and sizes, using effective mass parameters. From the calculated single- and bi-excitonic DOS, the CM critical energies E_0 were obtained for all the structures considered. The results were found to be in good agreement with the estimates obtained with more detailed theoretical approaches. Furthermore, the level of confinement (strong vs weak) and both the absolute value of electron and hole effective masses and their ratio were found to play an important role in determining the size dependence of the CM FoM in different materials. This method was then used to explore the effect on the CM critical energies of elongation, up to sizes inaccessible to atomistic approaches. In all cases considered E_0 tends towards the theoretical absolute minimum of the CM onset of two bandgaps for sufficiently long rods. Elongation at constant cross section leads to an increase in the single-particle DOS, while keeping the bandgap nearly unchanged,

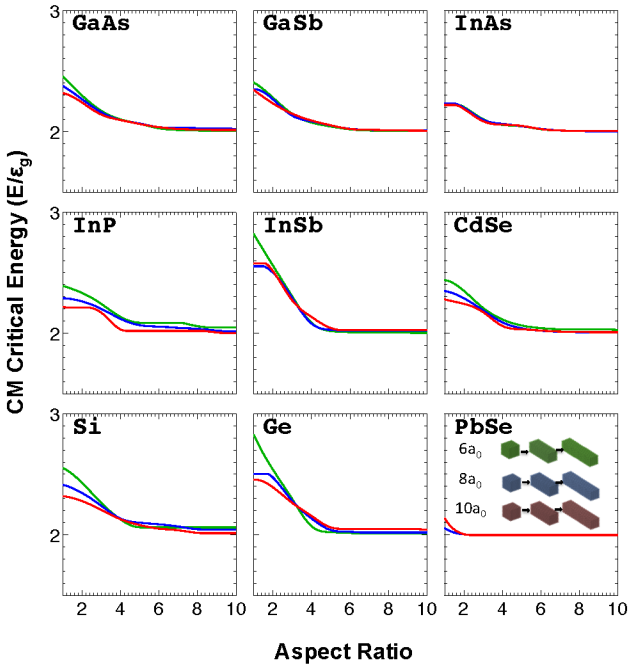

Fig. 10 Variation of (normalized) CM critical energies as a function of aspect ratio at constant volume, calculated for three different volumes: $6a_0^3$, $8a_0^3$ and $10a_0^3$.

making more states available in a given energy window. In structures elongated at constant volume the bandgap increases sharply due to the large decrease of the shorter axes, creating a larger energy window, and the resulting DOS is a consequence of the competition between the effects of decreased confinement along the elongation axis and of increased confinement across it. As a consequence, in the case of elongation at constant cross section (the case reflecting experimental growth conditions) the CM critical energy converges for smaller values of the aspect ratio, and, in many materials, exhibits a marked size dependence of the aspect ratio $\sigma_{\min}$ at which this convergence is achieved.

In summary, our results show that the origin of the decrease of the CM onset observed experimentally in elongated structures can be attributed purely to electronic structure effects, as surface-related effects, and effects due to both increased absorption and enhanced Coulomb coupling have been accurately filtered out in our investigation. This conclusion paves the way to the implementation of CM-efficiency-boosting strategies in nanostructures based on the lowering of the CM onset.

References

1 A. Nozik, *Physica E*, 2002, **14**, 115–120.
2 M. Hanna and A. Nozik, *J. Appl. Phys*, 2006, **100**, 074510.
3 R. D. Schaller and V. I. Klimov, *Phys. Rev. Lett*, 2004, **92**, 186601.
4 J. E. Murphy, M. C. Beard, A. G. Norman, S. P. Ahrenkiel, J. C. Johnson, P. Yu, O. I. Micic, R. J. Ellingson and A. J. Nozik, *J. A. Chem. Soc.*, 2006, **128**, 3241–3247.
5 R. D. Schaller, M. A. Petruska and V. I. Klimov, *Appl. Phys. Lett*, 2005, **87**, 253102.
6 J. Pijpers, E. Hendry, M. Milder, R. Fanciulli, J. Savolainen, J. Herek, D. Vanmaekelbergh, S. Ruhman, D. Mocatta, D. Oron *et al.*, *J. Phys. Chem. C*, 2007, **111**, 4146–4152.
7 M. C. Beard, K. P. Knutsen, P. Yu, J. M. Luther, Q. Song, W. K. Metzger, R. J. Ellingson and A. J. Nozik, *Nano Lett*, 2007, **7**, 2506–2512.
8 V. Sukhovatkin, S. Hinds, L. Brzozowski and E. H. Sargent, *Science*, 2009, **324**, 1542–1545.
9 O. E. Semonin, J. M. Luther, S. Choi, H. Chen, J. Gao, A. J. Nozik and M. C. Beard, *Science*, 2011, **334**, 1530–1533.
10 A. C. Bartnik, A. L. Efros, W. K. Koh, C. B. Murray and F. W. Wise, *Phys. Rev. B*, 2010, **82**, 195313.
11 J. A. McGuire, J. Joo, J. M. Pietryga, R. D. Schaller and V. I. Klimov, *Acc. Chem. Res*, 2008, **41**, 1810–1819.
12 V. I. Klimov, *J. Phys. Chem. B*, 2006, **110**, 16827–16845.
13 M. C. Beard, A. G. Midgett, M. C. Hanna, J. M. Luther, B. K. Hughes and A. J. Nozik, *Nano Lett.*, 2010, **10**, 3019–3027.
14 R. Schaller, M. Sykora, J. Pietryga and V. Klimov, *Nano Lett.*, 2006, **6**, 424–429.
15 R. D. Schaller, J. M. Pietryga and V. I. Klimov, *Nano Lett.*, 2007, **7**, 3469–3476.
16 M. Califano, A. Zunger and A. Franceschetti, *Nano Lett.*, 2004, **4**, 525–531.
17 A. Franceschetti, J. M. An and A. Zunger, *Nano Lett.*, 2006, **6**, 2191–2195.
18 G. Allan and C. Delerue, *Phys. Rev. B*, 2006, **73**, 205423.
19 R. D. Schaller, A. V. M. and V. I. Klimov, *Nature Phys.*, 2005, **1**, 189–194.
20 R. J. Ellingson, M. C. Beard, J. C. Johnson, P. Yu, M. O. P., A. J. Nozik, A. Shabaev and A. L. Efros, *Nano Lett.*, 2005, **5**, 865–871.
21 L.-W. Wang, M. Califano, A. Zunger and A. Franceschetti, *Phys. Rev. Lett.*, 2003, **91**, 056404–1–056404–4.
22 J. W. Luo, A. Franceschetti and A. Zunger, *Nano Lett.*, 2008, **8**, 3174–3181.
23 K. Hyeon-Deuk and O. V. Prezhdo, *ACS Nano*, 2012, **6**, 1239–1250.
24 J. M. An, A. Franceschetti, S. V. Dudiy and A. Zunger, *Nano Lett.*, 2006, **6**, 2728–2735.
25 S. Ithurria, M. Tessier, B. Mahler, R. Lobo, B. Dubertret and A. L. Efros, *Nature Mater.*, 2011, **10**, 936–941.
26 M. D. Tessier, C. Javaux, I. Maksimovic, V. Loriette and B. Dubertret, *ACS Nano*, 2012, **6**, 6751–6758.
27 K. P. Rice, A. E. Saunders and M. P. Stoykovich, *J. Amer. Chem. Soc.*, 2013, **135**, 6669–6676.
28 T. Mokari, M. Zhang and P. Yang, *J. A. Chem. Soc.*, 2007, **129**, 9864–9865.
29 Z. Quan, W. Siu Loc, C. Lin, Z. Luo, K. Yang, Y. Wang, H. Wang, Z. Wang and J. Fang, *Nano Lett.*, 2012, **12**, 4409–4413.
30 A. G. Midgett, J. M. Luther, J. T. Stewart, D. K. Smith, L. A. Padilha, V. I. Klimov, A. J. Nozik and M. C. Beard, *Nano Lett.*, 2013, **13**, 3078–3085.
31 P. D. Cunningham, J. E. Boercker, E. E. Foos, M. P. Lumb, A. R. Smith, J. G. Tischler and J. S. Melinger, *Nano Lett.*, 2011, **11**, 3476–3481.
32 P. D. Cunningham, J. E. Boercker, E. E. Foos, M. P. Lumb, A. R. Smith, J. G. Tischler and J. S. Melinger, *Nano Lett.*, 2013, **13**, 3003–3003.
33 R. L. Sandberg, L. A. Padilha, M. M. Qazilbash, W. K. Bae, R. D.

Schaller, J. M. Pietryga, M. J. Stevens, B. Baek, S. W. Nam and V. I. Klimov, *ACS Nano*, 2012, **6**, 9532–9540.
34 J. Yang, B.-R. Hyun, A. J. Basile and F. W. Wise, *ACS Nano*, 2012, **6**, 8120–8127.
35 L. A. Padilha, J. T. Stewart, R. L. Sandberg, W. K. Bae, W.-K. Koh, J. M. Pietryga and V. I. Klimov, *Nano Lett.*, 2013, **13**, 1092–1099.
36 M. C. Beard, J. M. Luther, O. E. Semonin and A. J. Nozik, *Acc. Chem. Res.*, 2012, **46**, 1252–1260.
37 G. Bryant and W. Jaskolski, *J. Phys. Chem. B*, 2005, **109**, 19650–19656.
38 I. Kang and F. W. Wise, *J. Opt. Soc. Am. B*, 1997, **14**, 1632–1646.
39 A. L. Efros and M. Rosen, *Annu. Rev. Mater Sci*, 2000, **30**, 475–521.
40 Y. H. Zhu, X. W. Zhang and J. B. Xia, *Phys. Rev. B*, 2006, **73**, 165326.
41 G. Zohar, R. Baer and E. Rabani, *J. Phys. Chem. Lett*, 2013, **4**, 317–322.
42 C. Delerue and M. Lannoo, *Nanostructures: Theory and Modelling*, 2004.
43 S. Lee, L. Jönsson, J. W. Wilkins, G. W. Bryant and G. Klimeck, *Phys. Rev. B*, 2001, **63**, 195318.
44 R. Viswanatha, S. Sapra, T. Saha-Dasgupta and D. Sarma, *Phys. Rev. B*, 2005, **72**, 045333.
45 F. Trani, G. Cantele, D. Ninno and G. Iadonisi, *Phys. Rev. B*, 2005, **72**, 075423.
46 J. Díaz and G. W. Bryant, *Phys. Rev. B*, 2006, **73**, 075329.
47 M. Korkusinski, O. Voznyy and P. Hawrylak, *Phys. Rev. B*, 2010, **82**, 245304.
48 L.-W. Wang and A. Zunger, *J. Chem. Phys.*, 1994, **100**, 2394–2397.
49 A. Canning, L. Wang, A. Williamson and A. Zunger, *J. Comp. Phys.*, 2000, **160**, 29–41.
50 J. Chelikowsky, *J. Phys. D*, 2000, **33**, R33.
51 A. Puzder, A. J. Williamson, G. J.C. and G. Galli, *Phys. Rev. Lett.*, 2002, **88**, 097401.
52 L.-W. Wang and J. Li, *Phys. Rev. B*, 2004, **69**, 153302.
53 M. Marsili, S. Botti, M. Palummo, E. Degoli, O. Pulci, H.-C. Weissker, M. Marques, S. Ossicini and R. Del Sole, *J. Phys. Chem. C*, 2013, **117**, 14229–14234.
54 M. Govoni, I. Marri and S. Ossicini, *Nature Photon.*, 2012, **6**, 672–679.
55 A. Kryjevski and D. Kilin, *Mol. Phys.*, 2014, **112**, 430–440.
56 M. Zieliński, *Phys. Rev. B*, 2012, **86**, 115424.
57 O. V. Prezhdo, *Acc. Chem. Res*, 2009, **42**, 2005–2016.
58 A. Yoffe, *Adv. Phys.*, 1993, **42**, 173–266.